

Physico-chemical modeling of the First Aerosol Characterization Experiment (ACE 1) Lagrangian B

2. DMS emission, transport and oxidation at the mesoscale

Céline Mari,¹ Karsten Suhre,¹ Timothy S. Bates,² James E. Johnson,² Robert Rosset,¹ Alan R. Bandy,³ Fred L. Eisele,⁴ R. Lee Mauldin III,⁴ Donald C. Thornton³

Abstract. A three-dimensional mesoscale meteorological model was used to study the interplay between the dynamical (turbulent mixing and advection) and physico-chemical (sea-air flux and photochemical sink by OH) processes that control dimethylsulfide DMS concentrations and their distribution in the marine boundary layer (MBL) during the First Aerosol Characterization Experiment ACE 1. Atmospheric DMS concentrations were constrained using observed seawater DMS concentrations and box model derived OH concentrations. Lateral boundary values of dynamical parameters were derived from the 6-hourly meteorological analysis of the European Centre for Medium-Range Weather Forecasts. Calculated DMS concentrations, wind speed and direction, and cloud cover were compared with measurements made aboard the R/V *Discoverer* and on the three NCAR/C130 aircraft flights during the LagB experiment. Model-generated atmospheric DMS concentrations agreed with the DMS observations from the NCAR/C130 aircraft flights during the LagB experiment ($R^2 = 0.69$) assuming OH is the only oxidant and DMS flux parameterization based on *Liss and Merlivat* [1986]. Comparison with Eulerian measurements made aboard the R/V *Discoverer* showed that the model simulated the range of observed values but not the hour-to-hour variation observed in the atmospheric DMS concentrations. Part of the discrepancy was attributed to uncertainties in DMS sea-to-air transfer velocity, small scale features of seawater DMS that are beyond the model resolution, and uncertainties in the venting of the boundary layer by shallow clouds. A quantitative budget at the ship location revealed a strong impact of advection processes in determining DMS levels and temporal evolution. The three-dimensional mesoscale meteorological model was also used to estimate the effect of the low spatial resolution used in global models on seawater DMS concentrations and atmospheric OH concentrations.

1. Introduction

Oceanic dimethylsulfide is thought to be the major source of non-sea-salt cloud condensation nuclei (CCN) in the remote marine troposphere and thus may play an important role in global climate regulation [Charlson *et al.*, 1987]. The climatic significance of this marine source of CCN is currently difficult to quantify due to an inadequate understanding of the chemical and physical processes linking seawater DMS concentrations with the formation and evolution of aerosol particles [Bates *et al.*, this issue (a)].

It is difficult from Eulerian observations alone to quantify the interplay of the various processes at work in the marine boundary layer (MBL). Lagrangian observations [Huebert *et al.*, this issue] and one-dimensional models [Suhre *et al.*, this issue] provide a framework to evaluate these chemical and physical processes in a specific air mass. However, they do not provide a mean to assess the regional and temporal variations of these processes. Three-dimensional models can fulfill this need as they integrate the controlling processes and feedbacks. In particular, three-dimensional models can respond to the need for spatial and temporal distributions of DMS and ultimately CCN by incorporating physico-chemical and dynamical processes in the same framework.

Here we present a three-dimensional (3-D) mesoscale meteorological model that was developed to investigate the relationships between the emission, atmospheric transport, chemical removal processes, and the resultant distribution of DMS during the ACE 1 LagB experiment. The model is applied over the limited oceanic area covered during the ACE 1 intensive study. The high spatial (20 km × 20 km) and temporal (time step 20 s) resolution of the model allows a direct comparison of the simulations with in situ observations

¹Laboratoire d'Aérodynamique, UMR CNRS/Université Paul Sabatier, Toulouse, France.

²Pacific Marine Environmental Laboratory, NOAA, Seattle, Washington.

³Department of Chemistry, Drexel University, Philadelphia, Pennsylvania

⁴Atmospheric Chemistry Division, National Center for Atmospheric Research, Boulder, Colorado

made on board the NCAR C-130 aircraft and NOAA ship *Discoverer*. On the basis of these comparisons, we evaluate two different DMS flux parameterizations that are frequently used: *Liss and Merlivat* [1986] (hereafter LM86) and *Wanninkhof* [1992] (hereafter W92).

One important aspect of the 3-D mesoscale model is the consideration of advection and turbulent mixing in the same framework. It has been suggested [*Leck and Persson*, 1996; *Liu et al.*, 1996] that dynamical processes such as turbulent mixing or wind speed affect observed DMS levels. *Bates et al.* [1990], *Andreae et al.* [1994] and *Ayers et al.* [1995] correlated high DMS concentrations with a sharp increase in wind speed which in turn affects the sea-air exchange rate. *Berresheim et al.* [1990] found a dramatic diurnal variation in measured DMS due to a decrease in MBL depth. Such observations confirm the short timescale response in atmospheric DMS levels to local variability in meteorological parameters, for examples changes in local wind speed or mixing depth in particular. Because of its lifetime (ranging from several hours to days), DMS can be advected over a fairly long distance. Advection of an air mass coming from a biologically productive region, richer in atmospheric DMS, may induce an increase of DMS concentrations at the location of measurement, without a local increase in wind speed or seawater DMS concentration. On the other hand, deeper turbulent boundary layers, advected toward a site of measurement results in a decrease in DMS concentrations without any local changes in the sea-air flux or oxidant concentrations. Thus there is a strong interplay between the relative effects of the sea-air flux, chemical oxidation by OH, turbulent mixing in the MBL, and advective transport on the atmospheric DMS distribution. In this paper we focus on these processes during the ACE 1 LagB experiment.

One major application of mesoscale models is to better understand the physical processes and to derive better subgrid parameterizations for global models. Consequently, mesoscale models are expected to play the role of intermediate tools between locally measured properties and global effects. From this point of view, one question is to address the sensitivity of global models to subgrid (mesoscale) processes. We address this question for the physico-chemical terms (sea-air flux and oxidation by OH) in two ways. First, we test the sensitivity of the model to different parameterizations of hydroxyl radical concentrations and sea-air flux with increasing levels of complexity: averaged hydroxyl radical (OH) from a global model and in situ OH from a box model, latitudinal seawater DMS spatial distribution, and seawater DMS distribution derived from measurements. Second, we derive the contribution of global model subgrid scale processes by doing spatial averaging on modeled mesoscale fields.

2. Model Description

2.1. Meteorological Model

The mesoscale model (Meso-NH) used in this study is a limited area meteorological model based on the Lipps and Hemler [*Lipps and Hemler*, 1982] modified anelastic system

of equations. Model physics and validation tests have been described by *Lafore et al.* [1998]. Only a short overview is presented here (see also *Suhre et al.* [this issue], for 1-D lagrangian simulations with the same model).

Meso-NH allows for on-line transport and diffusion of chemical components. Water vapor, clouds and rain water contents and scalar fields are advected online using a positive advection scheme. We use the Multidimensional Positive Definite Centered Difference method which insures the positiveness of the advection scheme by using a limiting factor for the advective flux (see *Lafore et al.* [1998] for more details). The calculation of the limiting factor is inspired from *Smolarkiewicz* [1989].

Subgrid scale transport, in particular transport due to cloud processes, is incorporated into the model in several ways. First, the turbulent state of the atmosphere is explicitly modeled using a prognostic equation for turbulent kinetic energy. The turbulent mixing (eddy) coefficients that are used to transport all model variables are set proportional to the square root of the turbulent kinetic energy and a mixing length l [*Stull*, 1988]. The eddy diffusion coefficient that is used for water vapor is applied for DMS. The mixing length l is determined as a nonlocal function of atmospheric stability by the distance that an air parcel with a given turbulent kinetic energy could travel upward or downward before being stopped by buoyancy [*Bougeault and Lacarrère*, 1989]. In the presence of clouds, vertical mixing is hence enhanced as condensational heating will release extra energy into the rising air parcel and thereby allow for larger mixing lengths. Various descriptions of appropriate length scales for eddies l - k have been suggested for differing cloud and cloud-free boundary layers. While *Bougeault et al.* [1981] indicated that a special formulation of the directionality and length of eddies was appropriate for unstable, broken cumulus cloud layers, the model used a universal formulation for simplicity. The penetrative effects of such cloud updrafts can cause substantial transports of tracers over a larger distance, an effect which ordinarily requires different equations than the diffusion terms used at the 20 km grid scale, or possibly, very specialized choices of l - k .

Second, a fractional cloudiness scheme is used in order to allow the simulation of clouds in a grid box which is not saturated on average [*Bechtold et al.*, 1992]. This is of particular interest for representing scattered cumulus clouds that would otherwise be ignored by the model. This scheme increases the activity of subgrid scale turbulent mixing in clouds (represented by the eddy diffusion coefficients) by means of the buoyancy flux term that appear in the turbulent kinetic energy equation. Third, the radiation scheme used in this model [*Morcrette*, 1989] calculates the visible and infrared upward and downward radiative fluxes. In the presence of stratocumulus clouds, infrared cooling at cloud top will lead to a destabilization of the potential temperature profile in the cloud and enhance turbulent transport in these regions. Fourth, a deep convection scheme [*Kain and Fritsch*, 1990] is used in order to model deep cumulonimbus convection. This scheme does not allow in its present version the transport of chemical species and is used here

only for the dynamical simulation. Although, both deep and shallow convective transport are certainly important in tropical regions [Chatfield and Crutzen, 1984; Wang *et al.*, 1995] and in midlatitudes [Chang *et al.*, 1987; Brost *et al.*, 1988; Brost and Chatfield, 1989], its impact should be minor during LagB. In fact, LagB was started well after the passage of a frontal system, and the convection scheme was never active within the LagB region at the time of the experiment. More recent work has been extended the analysis of the mass-flux (nonlocal) schemes for subgrid clouds transport of scalars [Siebesma *et al.*, 1995; Petersen *et al.*, 1998]; some of these formulations are particularly attractive for future inclusion in Meso-NH.

In clear-sky conditions, the boundary layer top is assumed to be at the altitude where modeled turbulent kinetic energy is reduced to $0.01 \text{ m}^2 \text{ s}^{-2}$. Under cloudy conditions, marine boundary layer height is assumed to go up to the top of the clouds. Lateral boundary conditions for meteorological variables are obtained through coupling with the large-scale fields provided by ECMWF analysis (every 6 hours), that incorporate in particular radiosoundings and surface observations made aboard the R/V *Discoverer*.

A diffusion operator is applied to the fluctuations of the prognostic variables (the fluctuations are defined here as the departure from the large scale value (see below)). The diffusion operator is a fourth-order operator used everywhere except at the first interior grid point where a second operator is substituted. A lateral sponge zone and a top absorbing layer are also defined in terms of fluctuations from large scale fields. During inflow conditions, boundary values for DMS are calculated, at each time step, as a weighted function of the five nearest grid points into the domain. The vertical model grid extends from the Earth's surface to the lower stratosphere and includes 62 altitude levels, with 38 of them below 3000 m, the first level being at 10 m, and the last one at 13 km. The horizontal resolution is $20 \text{ km} \times 20 \text{ km}$. The number of grid points in the horizontal x and y directions is 80×60 , thus covering an area of $1600 \text{ km} \times 1200 \text{ km}$. The domain is centered at 47°S – 141°E . The grid was chosen so that the LagB experiment is located in the southeastern part of this domain. On the basis of the average wind direction during the simulation period (westerly turning to northerly at the end of the period) and a DMS lifetime of 1 day in the MBL [Bates *et al.* [this issue (b)]], the air mass that was sampled during LagB had already spent at least one day in the model domain, which minimized the influence of boundary conditions.

Integration is performed with a time step of 20 s for a 50 hour period from December 7, 1995, at 0000 UTC to December 9, 1995, at 0200 UTC. This period includes a cold front passage through the domain, followed by clear-sky postfrontal conditions where the LagB experiment took place. We focus our attention on the last 29 hours, corresponding to the LagB period. The first 21 hours of the simulation is close to the spin-up time required for the model to forget initial conditions, in particular atmospheric DMS concentrations. A more improved version of the model is planned which will include coupling with a global model to

provide initial and boundary conditions for DMS concentrations at mesoscale.

2.2. DMS Production and Destruction in the Troposphere

The model creates its own DMS field from the transport, forced solely by the inputs of ECMWF data at the boundaries, the surface flux constrained by seawater DMS, and the oxidation by prescribed OH concentrations. Different parameterizations of seawater DMS, gas transfer velocity, and OH concentrations are implemented in the model. According to these parameterizations, we define four scenarios with a corresponding strategy: (1) a reference case, in which sea-air fluxes are calculated with measured seawater DMS concentrations and the LM86 transfer velocity parameterization, the OH diurnal cycle being derived from box model calculations accounting for modeled cloud cover; (2) a "global OH" case, in which OH radical concentrations are prescribed using monthly and zonally averaged values, similar to global models; (3) a "latitudinal DMS" case, similar to the reference case, but using zonally averaged seawater DMS distributions, similar to most global model approaches, and OH radical concentrations from the "global OH" case; (4) a "Wanninkhof" case, similar to the reference case, but using the W92 parameterization for gas transfer velocity. A full description of these four scenarios is given in the following sections.

2.2.1. Photochemical DMS oxidation. Although, there are still major uncertainties concerning atmospheric DMS chemistry, previous studies [Yin *et al.*, 1990; Turnispeed and Ravishankara, 1993; Berresheim *et al.*, 1995; Ravishankara *et al.*, 1997] have shown that OH is the dominant oxidizing agent for DMS in the clean and remote atmosphere. In this paper, we assume that DMS chemical consumption is solely due to oxidation by the OH radical. Atmospheric removal of DMS by reactions with NO_3 radicals are assumed to be negligible at the typically low NO_x concentrations encountered in the Southern Ocean (T. Carsey, personal communication, 1997). The rate of chemical loss L is given by

$$L = -k[\text{OH}][\text{DMS}]$$

where k is the rate constant [Hynes, 1986] and $[\text{OH}]$ is the hydroxyl radical concentration. Because of computational costs and in the absence of sufficient data to constrain a full chemical scheme in 3-D, we have chosen to prescribe OH concentrations. Two different parameterizations for OH have been implemented in the model.

The first method, corresponding to the reference case, adjusts the OH concentration based on the cloud cover calculated by the 3-D model. A box model is run under a set of configurations representing the different marine boundary layer and free troposphere conditions encountered during ACE 1. OH concentrations are then calculated as a function of cloud optical thickness using the radiation model from Madronich [1987] coupled with the box model. Figure 1 shows the sensitivity of modeled OH concentrations to variation in latitude and optical thickness. Between 41°S and 51°S , for a cloud optical thickness of 10, noon OH levels de-

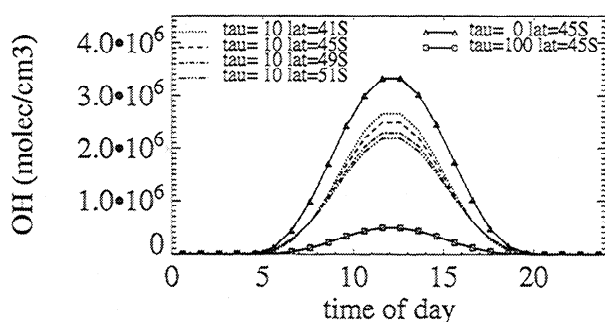


Figure 1. Results from box model calculations of the OH concentration in the MBL at local time of day. The OH diurnal cycle is represented for three values of optical thickness (0, 10, 100) at latitude 45°S and four values of latitude (41°S, 45°S, 49°S, 51°S) for a cloud optical thickness equal to 10.

crease by about 20% compared to clear-sky conditions. This decrease can be as high as 86% for an optical thickness of 100. At each time step and for every cloudy column in the model, optical thicknesses are deduced from modeled liquid water content following *Fouquart et al.* [1990]. Below- and above- cloud OH concentrations are then deduced from the previous box model calculations. The below-cloud OH concentrations are also used inside and up to the top of the cloud.

The second method uses monthly and zonally averaged OH concentrations for January, calculated from the 3-D photochemical model of *Spivakovsky et al.* [1990]. These concentrations are modulated with a semi-sinusoidal diurnal cycle. Such parameterization leads to an underestimation of OH concentrations in the marine boundary layer under clear-sky conditions since cloud effects are averaged over the 1 month period.

In Figure 2, both seasonal averaged and box model derived OH concentrations are compared with aircraft measurements during LagB. Flight 24 took place in a clear air mass, starting on December 7 at 1947 UTC and ending on December 8 at 0421 UTC. Flight 26 was cloudy starting from December 8 at 2001 UTC and ending on December 9 0352 UTC. Comparison in Figure 2 clearly shows an underestimation of the OH values by the first method (seasonal average) during Day of December (hereafter DOD) 8.0 (about 53% lower than the box model concentrations), whereas box model results are in good agreement with the measurements. On the other hand, during DOD 9.0 the seasonal averaged OH concentrations better fit the measurements. As will be shown in section 3., the model tends to overpredict the cloud water mixing ratio at the end of the LagB trajectory and consequently, the modeled cloud optical thickness. The high optical thickness obtained during DOD 9.0 (60) induces an underestimation of box model derived OH concentrations. OH concentrations are very sensitive to cloud optical thickness and thus to modeled liquid water content. Simulation of OH concentrations could be improved by the use of a detailed chemical scheme and radiative code in the 3-D model.

2.2.2. DMS emission at the sea surface. Up to now, no techniques have been successful for direct measurements

of the flux of DMS from the ocean to the atmosphere. Thus other methods have to be applied to estimate this flux. *Bates et al.* [1987a] derived an empirical relationship between DMS fluxes and the amount of solar radiation at the Earth's surface. According to this relationship, *Erickson et al.* [1990], *Benkovitz et al.* [1994] and *Pham et al.* [1995] derived the distribution of DMS emissions from the solar radiation in global models.

Langner and Rodhe [1991], *Feichter et al.* [1996] and *Chin et al.* [1996] calculated the oceanic DMS emissions as the product of latitude-averaged seawater DMS concentrations and sea-air exchange velocity. Here we calculate the DMS flux via this simple parameterization stating that the flux is determined by the product of the seawater DMS concentration and an exchange coefficient, which is calculated in the model as a function of the 10 m wind speed.

2.2.2.1. DMS exchange coefficient. We use two different sea-air transfer velocities, calculated from the model 10 m wind speed and sea surface temperature. The first one [*Liss and Merlivat*, 1986], used in the reference case, uses three linear equations, reflecting different modes of gas exchange as a function of wind speed. The second one [*Wanninkhof*, 1992] is based on the assumption of a quadratic dependence on wind speed. Both expressions of transfer velocity are derived for CO₂ fluxes and are scaled to DMS in the model using the Schmidt number [*Saltzman et al.*, 1993].

2.2.2.2. Seawater DMS concentrations. Seawater DMS concentrations were measured during the ACE 1 intensive operation period (November 15 to December 15, 1995) aboard the R/V *Discoverer*. The measurements covered a large region from 36°S to 56°S and 128°E to 161°E, including the model domain (see *Bates et al.* [this issue (b), Figure 1] for the whole area of measurements). As shown by the ship's route in Figure 3, measurements were unevenly distributed over the area. To constrain the value at the side boundaries before performing any interpolation, we deduced a latitudinal gradient of seawater DMS from the raw data.

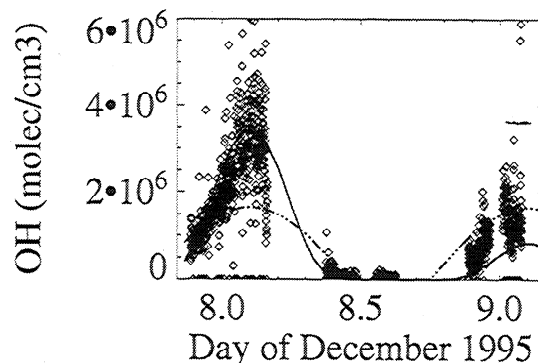


Figure 2. Results from measurements of OH concentrations during Lagrangian B flights (diamonds) at UTC. The measurement precision was 42%. The solid line represents the results from box model calculations for modeled optical thicknesses of 0 and 60 for December 8 (cloud free) and December 9 (cloudy), respectively. The dashed line represents OH concentrations deduced from seasonal averaged data assuming a semi-sinusoidal diurnal cycle.

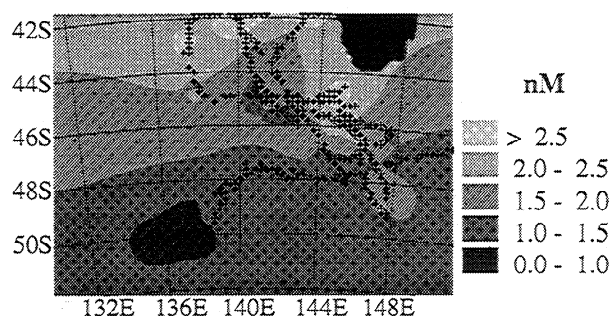


Figure 3. Seawater DMS concentrations from measurements made on board the R/V *Discoverer* during the intensive operations of ACE 1. Crosses represent ship's position where seawater DMS observations were performed. Concentrations are given in nM.

Figure 4 shows this latitudinal gradient as a linear regression of the averaged seawater DMS concentrations on 0.5° latitudinal intervals. This gradient was applied at the outer domain boundaries (at longitude 128°E and 161°E), whereas fixed values were applied along 56°S (0.14 nM) and 36°S (3.22 nM). With these boundary conditions added to the initial data set, an inverse distance averaging technique was carried out to interpolate data values on the grid. In this technique, points were weighted by the function $w = 1/d^2$ where d is the distance to the point. If several data points fell in the same grid cell, the value of that grid cell was the average of the several values. Figure 3 shows the result of the interpolation of seawater DMS on the model domain only. Note that we neglected the seasonal variation of DMS seawater concentration during the month of measurements [Bates *et al.*, this issue (b)].

3. Model Results and Comparison With Observations

Before testing the interplay between dynamical and physico-chemical processes that control DMS concentrations and their distributions in the MBL on the mesoscale, we test the ability of the model to reproduce measured DMS concentrations by comparing model results with data from

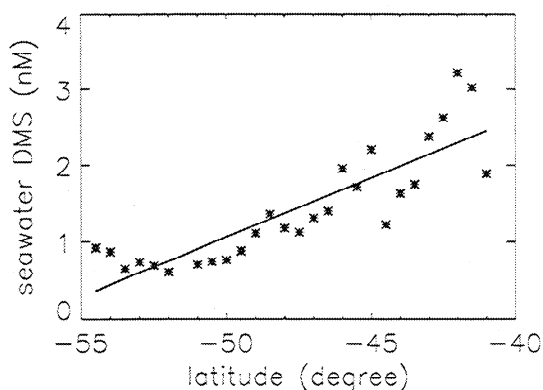


Figure 4. Latitudinal seawater DMS gradient (solid line) derived from a linear regression on 0.5° -latitudinal-averaged concentrations (stars).

the NCAR/C130 aircraft and the R/V *Discoverer* during the LagB period. Meteorological fields that play an important role in determining the DMS concentrations are discussed such as wind speed, wind direction, and cloud water. In this section, we present modeled time series of DMS fluxes, atmospheric DMS concentrations, and meteorological parameters following the ship and the Lagrangian trajectory.

3.1. Comparison With C-130 Observations

3.1.1. Meteorological fields. In order to assess the accuracy of the model-predicted Lagrangian trajectory, we have initialized a passive tracer at the beginning of LagB, at 45.5°S - 144.1°E on December 8 at 0200 UTC. The tracer was introduced with a maximum concentration at that point and a horizontal gaussian decrease over a 1° domain. The center of mass of that tracer was followed at 400 m above sea level, which corresponds to the mean level of the LagB balloons (Figure 5).

The tracer study shows good agreement between the modeled and observed trajectories which gives us confidence in the model's ability to correctly reproduce advective transport. In particular, the model is able to predict the sudden change in wind direction which occurred at 48.5°S - 146.3°E . Nonetheless, the tracer moves somewhat faster than the balloons and arrives at the end of LagB about 4 hours in advance of the balloons (on December 8 at 2200 UTC rather than on December 9 0200 UTC, i.e. 14% faster). In the following analysis, when comparing observed and simulated profiles, we extract model data following the trajectory of the tracer rather than the balloons. This strategy assures that we are actually looking at the same air mass from a model point of view, since this modeled air mass moves faster than the balloons. Flight 24 started before the balloon were launched. In order to compare our model results with all C-130 soundings, we extrapolated the tracer trajectory back to December 7 at 2100 UTC, just before the first aircraft sounding of flight 24. Comparison with observations is performed until December 8 at 2200 UTC which corresponds to the beginning of flight 26.

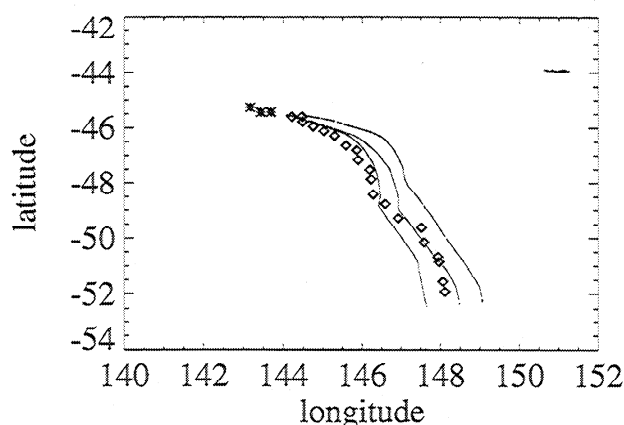


Figure 5. Trajectories of the three balloons during LagB. Diamonds represent the trajectory of the center of mass of a tagged air mass in the model. The trajectory was extrapolated to include the beginning of flight 24 (crosses).

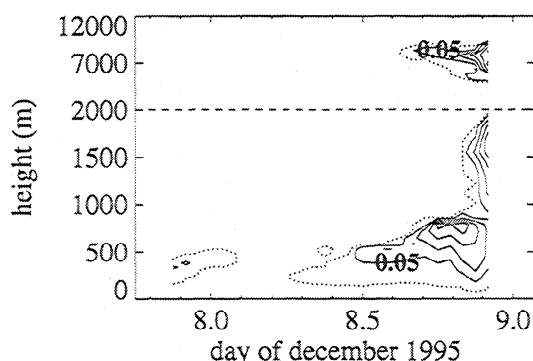


Figure 6. Simulated cloud water mixing ratio in g/kg for height between 0 and 12 km, along the LagB trajectory. Vertical distributions are displayed from December 7 at 2100 UTC to December 8 at 2200 UTC. Contour intervals are 0., 0.05, 0.15, 0.25, 0.35, and 0.45 g/kg. The vertical grid increment is 500 m below 2000 m and 5000 m above. (See *Suhre et al.* [this issue, Figure 4]) for observations.)

Clouds play an important role in the parameterization of OH concentrations used in our model. Consequently, the ability of the model to correctly reproduce the presence of cloud is crucial. Figure 6 shows the modeled cloud cover. We found that it is in qualitative agreement with observed data (see *Suhre et al.* [this issue], for a presentation of the observed liquid water profiles). During flight 24, a thin cloud is simulated at low altitude (300 and 400 m) and persists until December 8 0000 UTC, with low cloud water mixing ratio (less than 0.05 g/kg). Then, clear sky is predicted until December 8 at 1200 UTC. According to the observations, no clouds were encountered during the flight 24. During the vertical sounding on December 8 at 2130 UTC in flight 25, clouds are predicted at the correct level (500 m) with a cloud water mixing ratio of 0.13 g/kg which is nearly twice the observed values (0.07 g/kg at 500 m). During the beginning of flight 26, the model predicts two cloud layers. The first one extends from 200 m up to 900 m with a maximum value of cloud mixing ratio (0.3 g/kg) at 700 m on December 8 at 2000 UTC. The mixing ratio then decreases to 0.15 g/kg at 500 m on December 8 2200 UTC. The second layer extends from 1000 to 2000 m with a maximum cloud water mixing ratio of 0.4 g/kg at 1700 m which is higher than the observed 0.25 g/kg. Two layers were actually observed during the late soundings of flight 26. Additional thick clouds are predicted at the upper levels, with cloud bases at 7500 m from December 8 at 1700 UTC, decreasing down to 5000 m on December 8 at 2200 UTC, in agreement with the aircraft observations. The C130 actually crossed an altostratus cloud layer during its descent to the balloons. The model is thus able to simulate the occurrence of clouds at the corresponding levels although it tends to overpredict cloud water mixing ratios along the LagB trajectory.

Wind speed is properly reproduced by the model: the median simulated-to-observed ratio (hereafter MSOR) is 1.1 (quartiles are 0.9 and 1.2). In particular, the model captures the increase in surface wind speed from 5 to 13 m/s during night of December 8. However, the model overestimates wind speed at the end of LagB by 15%, but still succeeds

in the simulation of wind direction (MSOR is 1.0, quartiles 0.9, 1.1).

We now turn to the comparison of atmospheric DMS profiles and temporal evolution obtained along the simulated trajectory with observations from the C-130.

3.1.2. Atmospheric DMS vertical profiles and temporal evolution. DMS profiles in the reference case are compared with the observations made up to 1.5 hours on either side of the modeled time for flights 24, 25, and 26 in Figure 7. The measurement precision was approximately 1 pptv. During flight 24, a mixed DMS rich MBL is simulated up to 500 m, in agreement with the measurements. Modeled concentrations in this DMS rich lower layer agree generally well with the observations during soundings 24A and 24X. MSOR of DMS concentrations below 500 m is 1.0 (quartiles 0.9 and 1.02) for sounding 24A and 0.95 (quartiles 0.8 and 1.2) for sounding 24X. For the last two soundings of flight 24, DMS concentrations under 500 m are underpredicted by 17% during sounding 24Y and 25% during sounding 24B. During flight 25, the DMS rich MBL has reached 600 m. Values in the DMS rich MBL compare well: MSOR is 1.0 (quartiles 0.9 and 1.1) for both soundings 25A and 25B. In flight 26, the model tends to underpredict DMS concentrations on December 8 at 2100 UTC. In the lowest 300 m, MSOR is 0.77 (quartiles 0.7 and 0.8).

A direct comparison of aircraft DMS observations with simulated DMS concentrations (Figure 8) gave a linear regression of model equal to $0.744 \times \text{observation} + 10.18$ with an $R^2 = 0.693$. The model-simulated concentrations are based on the assumption that OH is the only significant DMS oxidant. Any additional atmospheric DMS sink would require a respectively higher DMS ocean source. It is important to recall the considerable uncertainties in current estimates of sea-air flux of DMS. One major uncertainty in the simulation of atmospheric DMS concentration is generated by the problem associated with the calculation of the transfer velocity, particularly in regions where temporal and spatial variation can be significant as during ACE 1 experiment [Turner et al., 1996]. In this paper, we use the two most widely used parameterizations, LM86 and W92, which are expected to cover the range of possible values for transfer velocity [Liss et al., 1997]. Some authors [Bates et al., 1987b; Berresheim, 1987; Andreae, 1990] used the formulation of Smethie et al. [1985] to evaluate the transfer velocity. They found values which are about 25% higher than the LM86 method. Chin et al. [1998] found DMS concentrations 25% lower with LM86 than by using the parameterization of Tans et al. [1990]. More generally, most of the formulations, based on experimental approaches, give results that broadly agree within a factor of 2. Recent studies have demonstrated that it is difficult to use wind speed alone to determine the sea-air exchange [Chin et al., 1998]. It has been proposed that other parameters such as surface temperature, but also sea state, sea surface microlayer, sea surface organic films, chemical reactions in surface seawater, thermal stability, and other parameters that are not yet identified could control the sea-to-air transfer velocity. The details of how these parameters influence the transfer velocity are not clearly understood

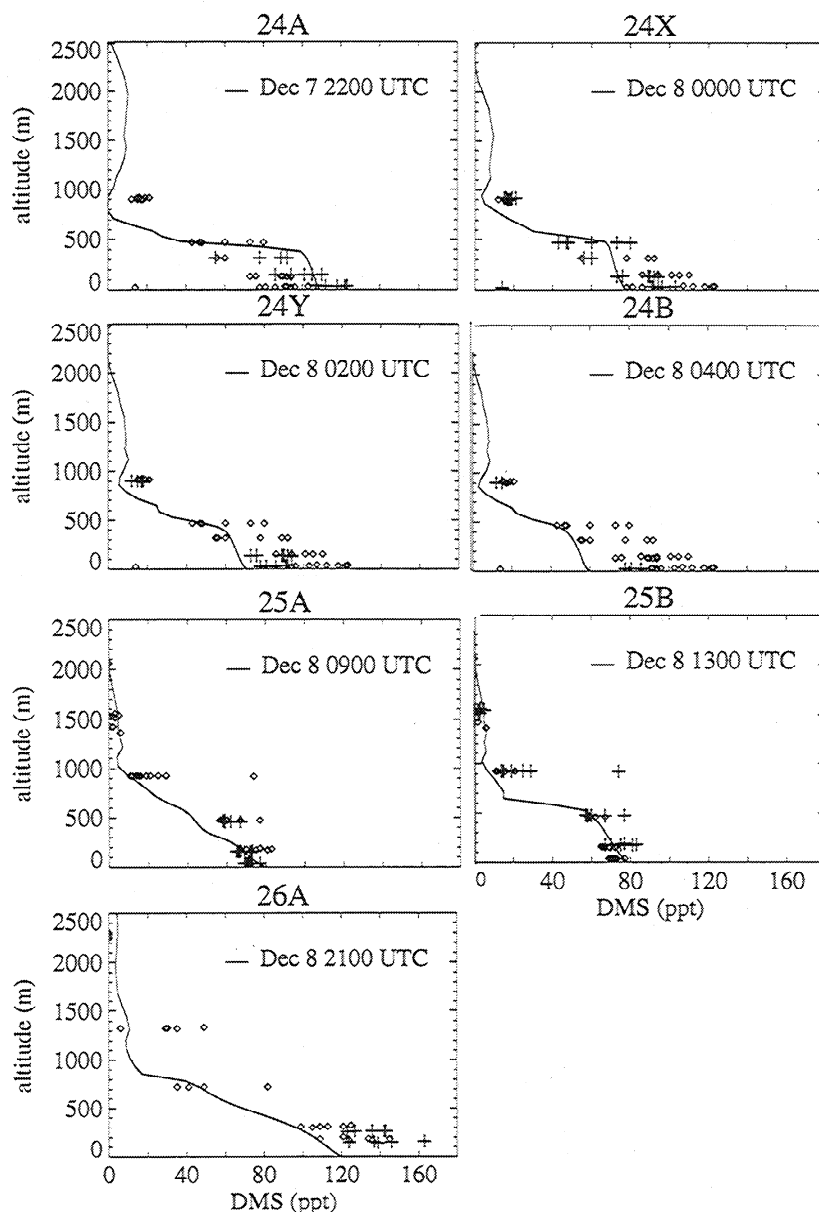


Figure 7. Vertical profiles of predicted DMS concentration (reference case) for each aircraft sounding during LagB (LDT equal to UTC + 1100). Diamonds are DMS concentrations measured aboard the NCAR/C130 during each specific flight. Crosses are DMS concentrations measured at 1.5 hours on either side of the modeled time. Concentrations are given in pptv. Measured DMS concentrations have a precision of 1 pptv. (See also *Suhre et al.* [this issue, Figure 12]).

[Erickson, 1993]. Further work needs to be done on the determination of transfer velocity to improve the parameterization of sea-air flux in regional and global model.

Major differences between modeled and observed profiles in Figure 7 occur above the mixed DMS rich layer (between 500 and 1200 m). This may be a result of insufficient cloud transport within the marine boundary layer. The model simulates a second layer of higher concentrations (about 10 pptv) at 1500 m. During sounding 25B, low values of DMS (5 pptv) were measured at 1500 m which are well reproduced by the model in this upper layer. DMS at this upper layer could have been advected from other areas influenced by convective upward transport [Eisele and McMurry, 1997; Chatfield and Crutzen, 1984; Ferek et al., 1986] by the low-

level clouds actually observed in the area [Hainsworth et al., this issue].

A portrayal of the Lagrangian is presented on Figure 9. Modeled seawater DMS, DMS flux, and wind speed at the surface are illustrated in Figure 9a. Note that during the LagB experiment, *Discoverer* remained at the beginning of the lagrangian trajectory. The ship started moving south-east on December 9, 1 day after the Lagrangian experiment started. Thus observations of seawater DMS shown in Figure 9a have been collected on DOD 9.0 along the LagB trajectory. The prescribed and measured seawater DMS concentrations compare well with MSOR 1.1 (quartiles 0.9 and 1.4) although the seawater DMS concentrations in the model strongly underpredict measurements between DOD 8.05 and

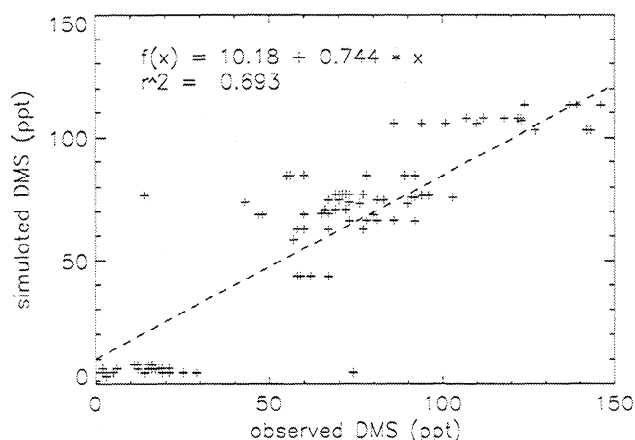


Figure 8. Comparison of aircraft observations with model-simulated DMS concentrations covering the period from sounding 24A to 26A. Model results were stored every 1 hour for each model level at the center of the tracer mass. All observations were then compared with closest stored model results.

8.2. Seawater DMS concentrations decrease from 2.5 nM on December 8 at 0500 UTC to 1.2 nM on December 8 at 2200 UTC below the Lagrangian trajectory as the air mass is moving toward higher latitudes. In contrast, wind speeds at the surface increase from 5 to 14 m/s at the same time leading to an enhancement of the sea-air flux from $0.5 \mu\text{mol m}^{-2} \text{d}^{-1}$ to $5 \mu\text{mol m}^{-2} \text{d}^{-1}$.

Variations in atmospheric DMS concentrations over the 26 hour period of LagB (at different levels below 1200 m) show that the model is able to capture time changes at a small scale (Figure 9b). Below 250 m, atmospheric DMS concentrations strongly reflect the variation of sea-air flux. DMS emissions and atmospheric concentrations both increase from Dec 8 at 0330 UTC. Modeled concentrations slightly underestimate the observations (MSOR is 0.9, quartiles 0.8 and 1.0). Above 250 m and below 500 m, similar behavior is simulated in agreement with observations (MSOR is 1.0, quartiles 0.9 and 1.3). Above 500 m and below 1200 m, average DMS concentrations slightly increase until DOD 8.0 as the MBL thickens (due to enhanced turbulent mixing) transferring DMS to higher altitudes. DMS concentrations then slowly increase as sea-air flux increases (MSOR reaches 1.1, quartiles 0.9 and 1.5).

The modeled atmospheric DMS concentrations are highly dependent on the wind speed transfer velocity relationship used to calculate the air sea exchange of DMS. The "Wanninkhof" case shows a significant overprediction of atmospheric DMS concentrations near the surface (Figure 9c). "Global OH" and "latitudinal DMS" parameterizations result in atmospheric DMS concentrations that are very similar to the reference case (Figure 9c). Thus a latitudinal distribution already captures the essential feature of the seawater DMS distribution when following the LagB trajectory. The MSOR is 1.0 for "global OH" case (quartiles 0.9 and 1.3) and 1.1 in the "latitudinal DMS" case (quartiles 0.9 and 1.2). The reference case, the "global OH" and "latitudinal DMS" cases are nearly equal at the beginning of the LagB. Concentrations move apart later in the day due to the un-

derestimation of OH concentrations in the global approach. Lower values of OH concentrations in "global OH" case partly compensate for the underprediction of DMS emission during flight 24, and thus the "global OH" case compares

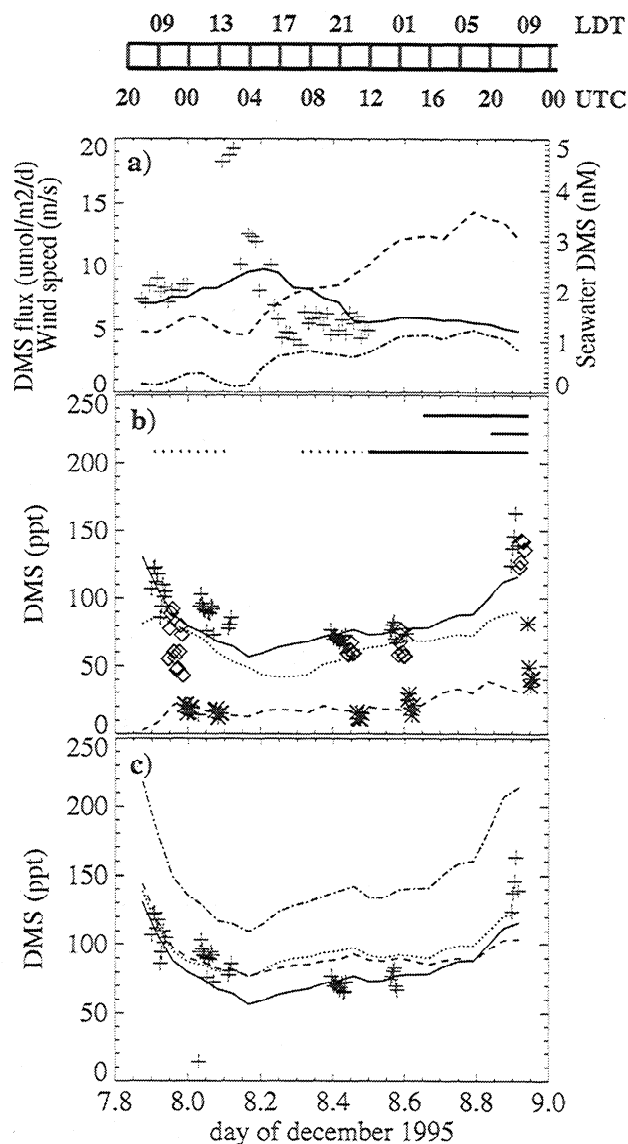


Figure 9. (a) Time series of modeled wind speed at the surface in m/s (dash-dotted line), DMS sea-air flux in $\mu\text{mol m}^{-2} \text{d}^{-1}$ (dashed line), and seawater DMS in nM (solid line), along the LagB trajectory. Crosses are the seawater DMS concentrations observed aboard the R/V *Discoverer* on Dec 9, as the ship started moving southeast, one day after the Lagrangian experiment started. (b) Time series of DMS concentrations in pptv during LagB. Comparison between model results (lines) and aircraft observations for the reference case at different altitudes: below 250 m (solid line and crosses), and between 250 and 500 m (dotted line and diamonds), between 500 and 1200 m (dashed line and stars). Bars represent clouds incidence by levels (see Figure 6). (c) Time series of DMS concentrations in pptv during LagB. Comparison between model results (lines) and aircraft observations below 250 m for different scenarios: reference case (solid line), "Wanninkhof" case (dash-dotted line), "latitudinal DMS" case (dotted line), and "global OH" case (dashed line). (See also *Suhre et al.* [this issue, Figure 20])

better to measurements than the reference case during this period. During the night (DOD 8.4 to 8.8), when the chemical loss by OH vanishes, the three simulated DMS concentrations tend to be close to each other. The MSOR in the reference case is 0.9 (quartiles 0.8 and 1.0). Thus discrepancies between "global OH", "latitudinal DMS", and reference cases are not very significant when following the LagB air mass trajectory. However, there are other regions in the modeling domain where the differences become important, as will be discussed in section 5.

On the basis of the correct representation of the LagB trajectory by the modeled tracer, we conclude that the dynamical processes are well described by the model when looking at the air mass from a Lagrangian point of view. Comparisons between measured and modeled DMS concentrations show that the model tends to underestimate systematically the observations by 10 to 25% in the well mixed layer near the surface. A source of underestimation of atmospheric DMS may be the uncertainties on DMS emissions due to both fine scale variations of seawater DMS concentrations and parameterization of transfer velocity. We discuss this point below.

3.2. Comparison With the R/V *Discoverer* Observations

Comparison with the ship DMS measurements is more difficult as we now add the complication of an Eulerian reference frame which needs to account for advection.

3.2.1. Meteorological fields. First, let us consider meteorology, beginning with the simulation of cloud water. Simulated clouds are responding to large-scale frontal processes. From December 7 at 2100 UTC to December 9 at 0200 UTC, the ship was located approximately at the starting point for the LagB experiment (45.5°S - 144.1°E). Pictures taken by the sky camera on the R/V *Discoverer*, radiosondes launched from the ship, and GMS satellite data showed scattered clouds over the ship after the front passage until Dec 7 at 2300 UTC, clear sky until Dec 8 at 0700 UTC, and overcast conditions for the remaining period. Figure 10 shows the temporal evolution of simulated cloud wa-

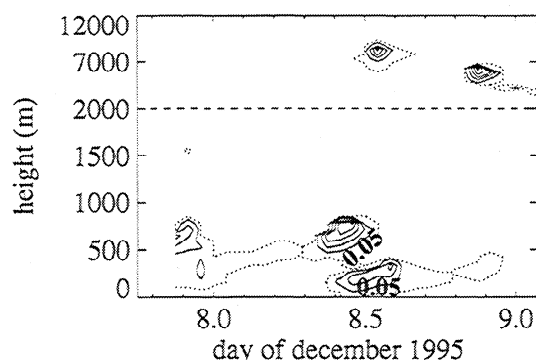


Figure 10. Simulated cloud water mixing ratio in g/kg for height between 0 and 12 km, along the R/V *Discoverer* trajectory. Vertical distributions are displayed from December 7 at 2100 UTC to December 9 at 0200 UTC. Contours intervals are 0., 0.05, 0.15, 0.25, 0.35, and 0.45 g/kg. Vertical grid increment is 500 m below 2000 m and 5000 m above.

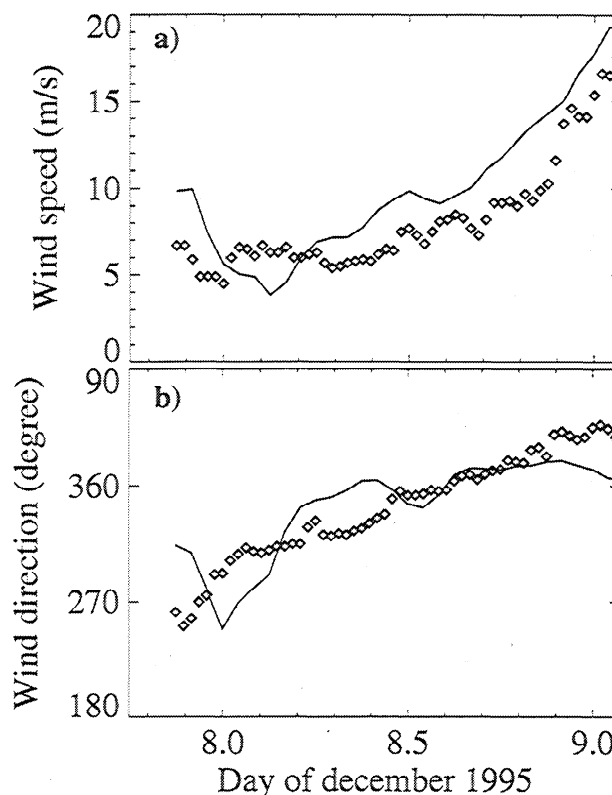


Figure 11. Modeled wind direction and wind speed at 10 m, along the R/V *Discoverer* trajectory, from December 7 at 2100 to December 9 at 0200 UTC (solid lines). Diamonds represent data from *Discoverer*. (a) Wind speed in m/s. (b) Wind direction in degrees.

ter mixing ratios along the ship track from the surface to 12 km. Cloud cover is qualitatively predicted at the beginning, followed by a clear-sky period. At night, MBL clouds form, until December 8 1400 UTC (day 8.6). High-altitude clouds are simulated from December 8 at 1200 UTC with cloud base decreasing from 7000 m to 3000 m at the end of LagB. According to radiosounding observations, clouds were observed on December 8 at 1200 UTC at 6000 m. The cloud base then decreased down to 3000 m on December 9 at 0000 UTC. Thus the model simulates the cloud cover over the ship correctly. However, toward the end of the period, high-altitude clouds are predicted at higher levels than actually observed.

The increase in wind speed and shift in wind direction as observed at the end of the LagB period are captured by the model as illustrated in Figure 11. Surface wind speed increases from 4 m/s at DOD 8.1 to about 20 m/s on DOD 9.0. The model tends to overpredict wind speeds at the surface with MSOR for wind speed equal to 1.3 (quartiles 1.1 and 1.4). Between DOD 8.0 and 8.2, however, the model underestimates the observations by about 20%. Simulated wind direction changes from northwesterly to northeasterly in agreement with the observations (MSOR is 1.0, quartiles 0.9 and 1.1). Major differences between observed and modeled wind direction occur on DOD 8.0 (45°) and DOD 8.35 (40°).

3.2.2. DMS flux. Now, let us return to the consideration of DMS fluxes. Although the model appears to capture

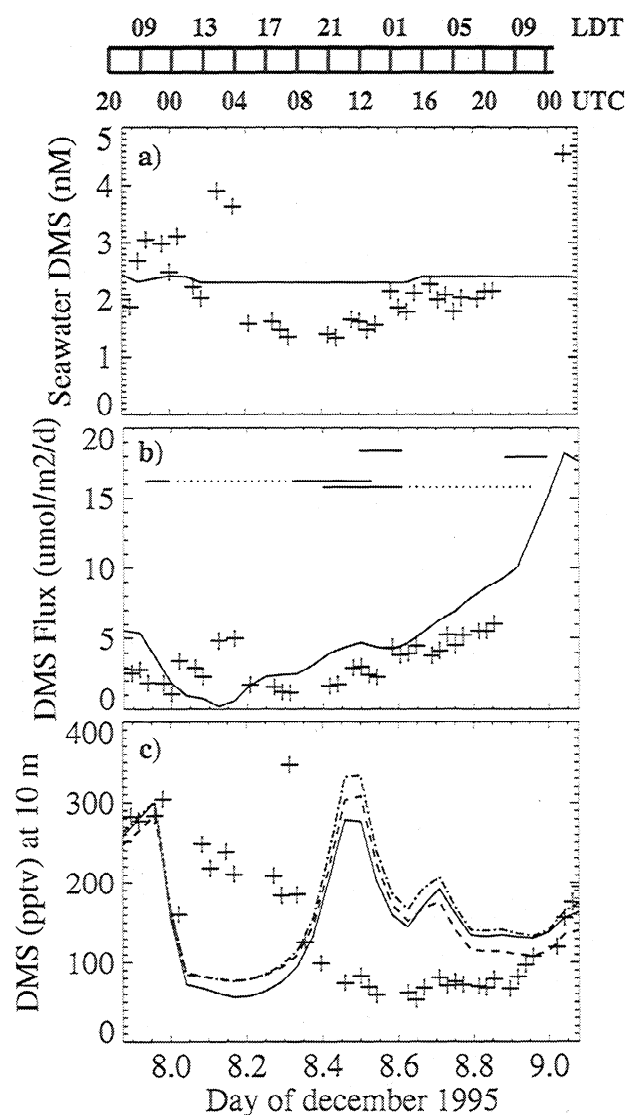


Figure 12. Time series along the R/V *Discoverer* trajectory from December 7 at 2100 to December 9 at 0200 UTC. Precision of atmospheric and seawater DMS concentrations measurements is $\pm 8\%$. (a) Seawater DMS concentration in nM in the model (solid line) and measured on board *Discoverer* (crosses). (b) Sea-air flux for reference case. Values are given in $\mu\text{mol m}^{-2} \text{d}^{-1}$. Crosses are fluxes calculated from measured seawater DMS and wind speed. Bars represent clouds occurrence by levels (see Figure 10). (c) Atmospheric DMS concentration in pptv for reference case (solid line), "latitudinal DMS" case (dashed line), and "global OH" case (dash-dotted line). Crosses are measured DMS concentrations.

many important features of the meteorological variables observed aboard *Discoverer*, it is unable to predict the hour-to-hour variation of atmospheric DMS concentrations and fluxes calculated from measurements. The predicted flux is generally higher (MSOR is 1.5, quartiles 1.2 and 1.8) than the DMS flux calculated from observed wind speed, DMS seawater concentrations, and using LM86 [Bates *et al.*, this issue (b)] with the exception of DOD 8.0 to 8.2, when the predicted flux was only 25% of the calculated flux (Figure 12). The lack of agreement in the calculated and predicted

DMS fluxes is likely a result of the spatial heterogeneity in DMS concentrations in this region. During LagB, the ship was in an area of strong DMS gradients in both the atmosphere and the ocean. Sharp gradients in salinity and SST in the region $45.3^{\circ}\text{S} - 46.0^{\circ}\text{S}, 145.0^{\circ}\text{E} - 145.5^{\circ}\text{E}$ indicate the mixing of subantarctic and polar water masses [Bates *et al.*, this issue (b)]. Comparison between measured seawater DMS concentrations and seawater DMS actually used in the model (MSOR is 1.2, quartiles 1. and 1.4) reveals a large range of concentration from 1.3 nM to 4.7 nM for measured concentrations (Figure 12a). Seawater DMS values introduced in the model remain around 2.35 nM and represent an average over all observations in that region. Observations can be up to 50% higher or lower than the values used in the model, which does not account for the heterogeneities in the seawater DMS distribution that are beyond its spatial resolution.

3.2.3. DMS temporal evolution. The atmospheric DMS concentration measured at the ship is a function of the source and sink terms occurring upwind of the ship during the previous 1-2 days. The concentrations measured at the ship during the period DOD 7.7-9.1 are not consistent with a dominant photochemical sink. Minimum DMS concentrations are measured during nighttime when there is no oxidation by OH. The discrepancies between the purely chemical and the actual observed diurnal cycles of DMS are therefore dominated by dynamical processes and sea-air flux rather than photochemistry.

Atmospheric DMS measurements, taken at 17 m above sea level, and model results, in the first level (10 m), both fall within the range of 60-360 pptv. However, the model fails to reproduce the timing of the changes in DMS concentration. The limitation of the current model in interpreting hour-to-hour DMS observations is partly due to the uncertainties in parameterization of sea-to-air transfer velocity and subgrid-scale variations of seawater DMS as discussed above.

An additional explanation for the difference between modeled and observed DMS levels and temporal variation is the influence of advection processes. Modeled DMS concentrations fall from 300 pptv to 70 pptv in 2.4 hours at DOD 8.0. A budget calculation for the grid cell containing the ship location during this period shows a -263 pptv change in the atmospheric DMS concentration due to advection which is partly compensated by DMS emission (+48 pptv during the period). Photochemical oxidation by OH induces a change of -7 pptv which is well below the decrease due to advection terms. Similarly, between DOD 8.35 and 8.45, modeled atmospheric DMS concentrations increase from 110 to 280 pptv. During nighttime, photochemical oxidation plays a minor role with less than 2 pptv decrease in DMS concentrations during this 2.5 hour period. The sea-air flux term induces a +42 pptv increase of DMS concentrations. Advection is the major process as it increases the DMS concentration by 84 pptv. Thus the dramatic changes in modeled DMS concentrations during this period are a function of both the air-sea exchange and advection.

The two sudden variations in modeled atmospheric DMS concentrations occur when simulated and observed wind di-

rection show the largest differences. On DOD 8.0, the simulated wind direction is 250° (southwesterly), whereas the observed wind direction was 295° (northwesterly). Between December 7 at 2000 UTC and December 8 at 0200 UTC, the ship was located in a frontal region which was positioned along a northwest southeast direction. Consequently, southwesterly wind advects air from a zone of low DMS concentrations (less than 100 pptv) over the ship location. On the contrary, northwesterly winds, as observed on the ship, advect DMS from a region with higher DMS concentrations (more than 250 pptv). On DOD 8.3, the simulated wind direction is 360° (northerly) whereas observed wind direction was 320° (northwesterly). Northern winds advect the air mass from a rich DMS region toward the ship. Northwestern winds would have advected this air mass eastward at lower latitudes. The end result is a 40° difference between the modeled and observed wind direction can lead to a net difference in atmospheric DMS concentration as high as 150 pptv. Although a change in wind direction (advection) can explain the sudden variations in modeled DMS concentrations during this period, we have to acknowledge that the variations in the sea-air flux of DMS can have a similarly large effect. As discussed above, DMS seawater concentrations in this region varied from 1.3 to 4.7 nM. If we assume a constant average wind speed upwind of the ship of 6 m/s and an average DMS seawater concentration of 2.3 nM the resulting flux, assuming LM86 wind speed-transfer velocity relationship, would be $2.2 \mu\text{mol m}^{-2} \text{d}^{-1}$. Substituting this flux into the budget calculation described above results in a change of +280 pptv due to DMS emissions which is essentially equal to the change due to advection.

When model results are compared to Eulerian observations, one important consideration is that while the mesoscale model is expected to simulate gross features of large scale meteorological events reasonably well, the timing and location of each event are not likely to be simulated accurately [Liu *et al.*, 1996]. The comparison between model results and observations made on board R/V *Discoverer* demonstrates that inaccuracies in the meteorological data governing the transport direction and location and time of events inevitably lead to mismatch between the model and the observations [Benkovitz and Schwartz, 1997].

In conclusion, the budget calculation reveals that advection is a major factor in determining the DMS levels and temporal variation at the location of the ship and during this particular period. DMS emission appears to be the second most important factor in determining DMS concentrations.

4. DMS Regional Distribution

In order to determine the interplay of the parameters controlling atmospheric DMS concentrations at the mesoscale, we now look at the overall regional impact of the main processes such as the source flux (combination of seawater DMS and wind speed), the sink (oxidation by OH) and transport (turbulence and advection) terms.

It is worth emphasizing that the ACE 1 sampling situations contain considerable midlatitude weather features.

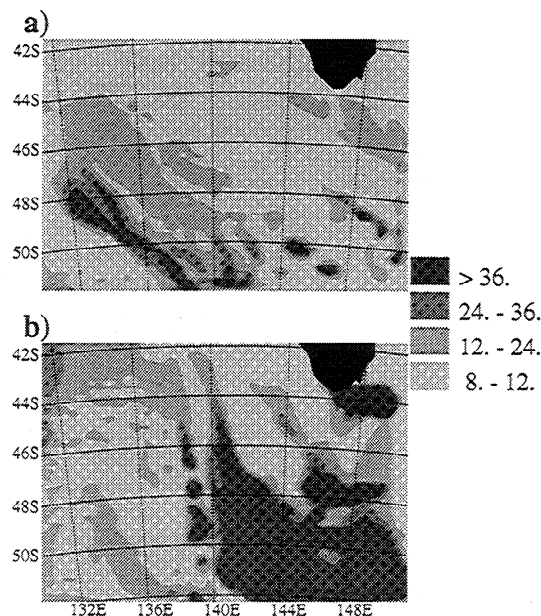


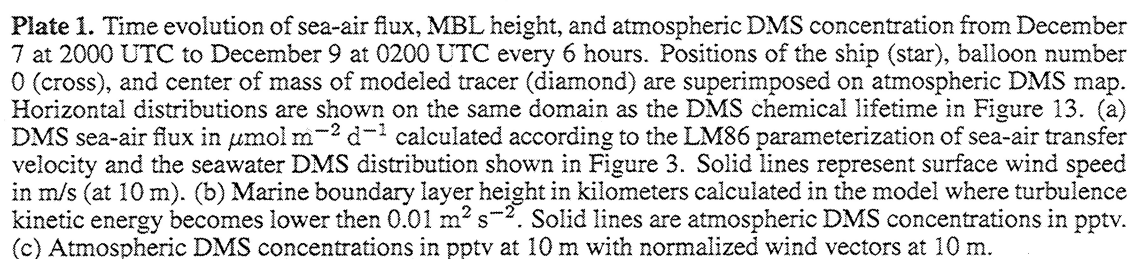
Figure 13. Horizontal distribution of "instantaneous" chemical DMS lifetime in hours on (a) December 8 at 0200 UTC and (b) December 9 at 0200 UTC. The increased lifetimes in Figure 13b are a result of the more extensive high-level clouds associated with the cold front which moved into the area.

During the early hours of December 8, clear air eventuates at most levels in the area of the LagB. Scattered low-level clouds were observed in the Lagrangian area until December 9 when more extensive high-level clouds associated with the cold front moved over the area (Figure 13). Airflow turned from eastward to southeastward at the end of the simulated period as a low moved southeastward off the Australian continent into the northern ACE 1 area (Plate 1c). This synoptic cyclonic features influenced atmospheric DMS distribution as discussed below.

Temporal evolution of atmospheric DMS concentrations in Plate 1 shows a northwest/southeast structure of the field on December 7 at 2000 UTC, becoming northsouth on December 9 at 0200 UTC. In this section, we point out the complex interplay between mixing in the MBL, oxidation by OH, and sea-air flux that can lead to such a change in spatial distribution. We focus our attention on December 8 at 0800 UTC, December 8 at 1400 UTC and December 9 at 0200 UTC.

4.1. DMS Chemical Lifetime

In order to discuss the role of oxidation by OH, "instantaneous" DMS chemical lifetime distributions are calculated near the surface based on the box model derived OH concentrations. Because of our parameterization of OH, the DMS lifetime strongly reflects the presence of clouds in the area. Simulated clouds covered 30% of the entire domain on December 8 at 0200 UTC resulting in a mean "instantaneous" lifetime of 13 hours (Figure 13a). On December 9 at 0200 UTC, 53% of the sky was cloudy, with most of the clouds located in the southeast portion of the domain. The result-



ing "instantaneous" mean lifetime of DMS in the MBL is 25 hours (Figure 13b). Note that these values are calculated during the early afternoon when the chemical loss is high and thus the actual lifetime is approximately twice as long. However, the calculated distributions illustrate that the DMS chemical destruction rate can vary by a factor of 10 within the model domain. Similarly, the DMS flux and MBL height can vary by a factor of 10 and 20, respectively (Plate 1).

4.2. December 8 at 0800 UTC

On December 8 at 0800 UTC, a patch of atmospheric DMS rich air is located south of Tasmania (44.5°S, 144°E). DMS concentrations are greater than 250 pptv. There is no evidence of an important local source. In this region, the DMS flux is low (less than $4 \mu\text{mol m}^{-2} \text{d}^{-1}$). The MBL height is around 1 km. The slow DMS loss rate at this time (sunset) is expected to partially explain the high DMS concentrations but cannot explain the location of this maximum. Obviously, this maximum may have been advected from a region of higher DMS concentration located to the north. Such region appears on December 7 at 2000 UTC around (42°S, 140°E). Although seawater DMS concentrations in this northern region are high, the DMS flux on December 7 at 2000 UTC is relatively low due to lower wind speeds. However, the low MBL height (below 500 m) counteracts the low flux and thus increases the atmospheric DMS concentration near the surface. This region is then advected southeastward toward the ship location.

4.3. December 8 at 1400 UTC

Additional evidence of advection can be identified on December 8 at 1400 UTC. A tongue of high atmospheric DMS concentrations is located along a northwest/southeast axis (49°S, 134°E and 52°S, 138°E). Along this axis, the DMS flux is very low (less than $2 \mu\text{mol m}^{-2} \text{d}^{-1}$). The MBL height is between 500 m and 1 km. Loss by oxidation is slow (nighttime). An additional source of DMS appears to be the southward advection from a region of high DMS concentrations. This region of DMS concentrations greater than 150 pptv is shown on December 8 at 0200 UTC. It is the result of a high DMS flux (more than $3 \mu\text{mol m}^{-2} \text{d}^{-1}$) and low DMS oxidation due to the presence of clouds. Note that this region of maximum atmospheric DMS concentrations corresponds to low seawater DMS concentrations.

4.4. December 9 at 0200 UTC

The modeled atmospheric DMS field on December 9 at 0200 (Plate 1) reveals a strong east-west gradient located at 140°E (more than 100 pptv in 80 km distance). The seawater DMS distribution, however, (Figure 4) is dominated by a north-south gradient. Multiplication by the transfer velocity hides this latitudinal distribution, and the DMS flux more closely reflects the wind speed distribution near the surface. The eastern part of the domain is thus characterized by a high DMS flux (more than $4 \mu\text{mol m}^{-2} \text{d}^{-1}$). This effect is emphasized further by a low MBL height in this part of the domain (between 500 m and 1 km). In addition to

these two processes, a low chemical loss (DMS lifetime is greater than 1 day) contributes to maintain high DMS concentrations. The region located west of longitude 140°E on December 9 at 0200 is characterized by a higher chemical loss rate (DMS lifetime lower than 24 hours). Furthermore, clouds appear in the north leading to a higher MBL height (higher than 2 km, whereas it is lower than 1.5 km to the south). High MBL heights induce a more effective dilution of the DMS and thus offset the effect of a strong DMS flux in the same region. Finally, the combination of the north-south gradients of MBL mixing and DMS flux creates a uniformly DMS poor region west of longitude 140°E.

Thus we see that atmospheric DMS at the mesoscale is a result of the complex interplay between emission, oxidation, vertical mixing, and transport processes. These processes are competitive and can counteract each other. All these processes are "subgrid scale" to a global model with a typical horizontal resolution of 2° to 6°. Thus they need to be carefully parameterized, especially when deriving sulfate aerosol formation from the modeled DMS distribution. A mesoscale model as presented here is appropriate to develop and test such parameterizations as will be shown in the following section.

5. Scaling up From the Mesoscale to the Global Scale

Mesoscale models provide a mean to test common global model assumptions such as coarse OH and DMS seawater distributions. Model comparisons with the R/V *Discoverer* observations showed that there were no significant differences between the "latitudinal DMS", "global OH", and reference cases. We now look at the atmospheric DMS distribution in the entire domain to see if there are some regions where the differences are higher. Comparisons using the "latitudinal DMS" and "global OH" distributions show a relative difference in atmospheric DMS concentrations ranging from -10 to 10% in 76% of the domain (including LagB trajectory) on December 9 at 0200 UTC. However, in regions where latitudinal seawater DMS concentrations are 20% lower than seawater DMS concentrations derived from measurements, the "global OH" case (accounting for seawater DMS concentration fine structures) gives DMS concentrations 25% greater than the "latitudinal DMS" case. Differences between the fluxes can reach $+8 \mu\text{mol m}^{-2} \text{d}^{-1}$, leading to differences in atmospheric DMS concentrations that can locally reach 100 pptv.

The effect of clouds on the OH parameterization induces changes in the oxidation rate, as the hydroxyl radical concentration may substantially decrease. On December 9 at 0200 UTC, atmospheric DMS concentrations from reference and "global OH" cases differ from -10 to +10% in 74% of the domain. In a relatively cloud free region in the southwest sector of the domain, OH concentrations derived from the box model are about 60% higher than monthly and zonally averaged OH concentrations. In this region, the reference case gives atmospheric DMS concentrations more than 25% lower than the "global OH" case. Similar results were ob-

tained for December 8 at 0200 UTC. In summary, changes in atmospheric DMS concentrations induced by the different scenarios of chemical oxidation and sea-air flux are less than 10% in the major part of the ACE 1 domain. Locally, the difference can reach 25% under clear sky or when the difference between averaged seawater DMS concentrations and measured seawater DMS concentrations is greater than 20%.

To quantify the effect of spatial averaging in numerical model we evaluate what we call here the subgrid-scale term. This strategy is adapted from the scaling-up technique used to evaluate the contribution of eddy terms at mesoscale [Bechtold *et al.*, 1996] and to quantify the problem of spatial averaging in photochemical models of the stratosphere [Pyle and Zavody, 1990].

Let $[DMS]_{aq}$, $[OH]$, and $[DMS]$ denote the concentrations of seawater DMS, hydroxyl radical and atmospheric DMS, k_w the transfer velocity, and k the rate constant. Suppose that X is the true value. The quantity \bar{X} denotes the spatially averaged values, that is, the values actually used by global models. The quantity X' is the fluctuation or departure from the true value. Consider the sea-air flux, $k_w [DMS]_{aq}$, and the reaction rate $k [OH] [DMS]$. The spatial average for these terms is given by

$$\frac{k[OH][DMS]}{k_w[DMS]_{aq}} = \frac{k[\bar{OH}][\bar{DMS}]}{\bar{k}_w[\bar{DMS}]_{aq}} + \frac{k[OH'] [DMS']}{k'_w [DMS']_{aq}}$$

The term on the left we call the true rate. The first term on the right is the rate which would be calculated in a global model. The true rate and the global model rate are not, in general, equal. The difference between the true rate and the global model rate reveals the subgrid scale variations. For a global model point of view, the subgrid scale term represents the contribution of mesoscale variations to the true rate. In order to evaluate this contribution, a spatial averaging is performed on a box located over the Lagrangian trajectory start point. The box is chosen to be $6^\circ \times 6^\circ$ and 60 m high, close to a global model grid [e.g., Feichter *et al.*, 1996].

Using this approach, the calculated values of the subgrid-scale term of sea-air flux are low, ranging from -0.5% on December 7 at 2000 UTC to -4% on December 8 at 0800 UTC of the true rate. Thus, at that particular grid point, the global model rate is greater than the true rate. Similarly, the calculated subgrid-scale term for loss by OH is always negative, ranging from -2% (on December 8 at 0800 UTC) to -10% (on December 8 at 2000 UTC) of the true rate. Moving the box in several regions on the model domain gives values for subgrid-scale term between -10 and +10%. Although this contribution is not significant, it should not hide the importance of the subgrid scale variability when studying the sulfur cycle. Benkovitz *et al.* [1994] demonstrated that a horizontal grid spacing of approximately 1° is required to capture the spatial variability of the sulfate concentrations over the central North Atlantic. The present work may be used in the future to evaluate and develop subgrid-scale parameterizations of this variability for global scale models.

6. Conclusions

Atmospheric DMS concentrations were simulated with a mesoscale model during the ACE 1 LagB experiment. Model results were compared with measurements made aboard the R/V *Discoverer* and NCAR C-130. Comparison with the aircraft data was made with results obtained along a tagged parcel of air released in the model. This strategy involved a Lagrangian analysis of the Eulerian model output at mesoscale. The model was found to correctly reproduce the observed LagB trajectory. Furthermore, over 50% of the model calculated atmospheric DMS concentrations were within a factor of 0.7 and 1.5 of the measured DMS concentrations on the NCAR/C-130 when using the combination of LM86 parameterization of air-sea exchange and the chemical loss deduced from prescribed concentrations of OH derived from a box model. In most case, the comparison shows that the model tends to underestimate the DMS observations in the marine boundary layer by 10 to 25%. The measured and modeled atmospheric DMS concentrations were in closest agreement when using the Liss and Merlivat [1986] sea-air exchange parameterization. However, this conclusion is based on the assumption that OH is the only significant DMS oxidant. Any additional atmospheric DMS sink would require a higher DMS source from the ocean. We also acknowledge that cloud transport may be underestimated in the model. A more vigorous cloud transport also would require a higher DMS source from the ocean.

Comparisons were also made in a Eulerian framework with measurements from the R/V *Discoverer*. There was fair agreement between observed and modeled wind and cloud cover. Calculated DMS sea-air flux temporal evolution in the model captures the essential features of calculated DMS sea-air flux from observations. Although the model was able to reproduce the range of measured atmospheric DMS concentrations, the model did not reproduce the hour-to-hour DMS concentration variations most likely due to the strong horizontal gradients of DMS in both the atmosphere and the ocean.

Uncertainties in DMS emissions and advection processes are the major sources of the discrepancy. In one case, a minor difference between the modeled and measured wind direction (40°) was shown to induce very different modeled and observed atmospheric DMS concentrations (150 pptv). The discrepancies between model results and shipboard observations emphasize the need to accurately represent dynamics (wind speed and direction) in mesoscale models in order to interpret the observed DMS variations. Overall, the present model was able to create atmospheric DMS concentrations without any other constraint than the observed seawater DMS concentration, box model derived OH concentrations and ECMWF analysis for lateral boundary values of dynamical parameters. A better evaluation of the model will require comparing model results with observations of DMS oxidation products such as SO_2 and sulfate. Such a comparison will provide a more constrained evaluation of model processes such as emission flux, oxidation rate, boundary layer mixing and advection. Future work will add DMS oxidation

products and aerosols into this 3-D framework (C. Mari et al., manuscript in preparation, 1998). Aerosol microphysics, chemistry, and optical measurements made during ACE 1 will then be used to test and validate model results.

On a regional scale, boundary layer DMS concentrations were shown to be a complex interplay between dynamical and physico-chemical processes. Wind direction and speed were shown to be of particularly importance when studying DMS spatial distributions because of the advective transport of DMS rich air masses to regions where there were no important local sources. MBL thickness strongly influenced DMS distributions and concentrations. Increases (or decreases) in the MBL height were shown to counteract the effect of DMS flux enhancement (or decrease) on atmospheric DMS concentrations. Thus high temporal and spatial variability of atmospheric DMS concentrations can not be related to only local changes in sea-air fluxes or loss by OH oxidation.

All these processes are "subgrid-scale" processes to global models and need to be carefully represented. The mesoscale model was used to compare common global model assumptions such as coarse OH and seawater DMS concentration distributions. Comparisons were performed between two parameterizations of the hydroxyl radical (OH): box model derived and seasonally and zonally averaged concentrations. The results showed that average OH concentrations induced differences in atmospheric DMS concentrations between -10 and +10%. Under clear-sky conditions, atmospheric DMS concentrations varied by more than 25%. The mesoscale model was also used to compare two seawater DMS distributions: the first accounting for regional structures, based on in situ measurements, the second following a latitudinal variation. The fine structure in seawater DMS concentrations changed the atmospheric DMS concentrations by -10 to +10% in most of the model domain. The difference reached 25% when latitudinal seawater DMS concentrations were 20% different from seawater DMS derived from measurements. Finally, to estimate the effect of spatial averaging, we calculated the subgrid-scale (mesoscale) variations in a global model approach associated with loss by OH and DMS sea-air flux. The results showed that during ACE 1, subgrid-scale processes accounted for at most 10% of the true rate. This result, however, is specific to ACE 1 time and location. The present work may be used in the future to evaluate and develop subgrid-scale parameterizations of this variability for global scale models.

Acknowledgments. This research is a contribution to the International Global Atmospheric Chemistry (IGAC) Core project of the International Geosphere-Biosphere Programme (IGBP) and is part of the IGAC Aerosol Characterization Experiments (ACE). We gratefully acknowledge rapid access to all ACE 1 data via the UCAR/JOSS office. Of particular use for this study were smart balloon parameters from S. Businger, data on wind speed, temperature, and humidity from the NCAR/C130, and GMS and NOAA satellite images. Analysed synoptic scale meteorological data originate from the ECMWF archive MARS. Computing resources were provided by CNRS/IDRIS and Meteo France. Some financial support was provided by CNRS program PATOM and University Paul Sabatier.

References

- Andreae, M.O., Ocean-atmosphere interactions in the global biogeochemical sulfur cycle, *Mar. Chem.*, **30**, 1–29, 1990.
- Andreae, T.W., M.O. Andreae, and G. Schebeske, Biogenic sulfur emissions and aerosols over the tropical South Atlantic, 1, Dimethylsulfide in seawater and in the atmospheric boundary layer, *J. Geophys. Res.*, **99**, 22819–22829, 1994.
- Ayers, G.P., R.W. Gillett, J.P. Ivey, B. Schäfer, and A., Gabric, Short-term variability in marine atmospheric dimethylsulfide concentration, *Geophys. Res. Lett.*, **22**, 2513–2516, 1995.
- Bates, T.S., R.J. Charlson, and R.H. Gammon, Evidence for the climatic role of marine biogenic sulphur, *Nature*, **329**, 319–321, 1987a.
- Bates, T.S., J.D. Cline, R.H. Gammon, and S.R. Kelly-Hansen, Regional and seasonal variations in the flux of oceanic dimethylsulfide to the atmosphere, *J. Geophys. Res.*, **92**, 2930–2938, 1987b.
- Bates, T.S., J.E. Johnson, P.K. Quinn, P.D. Goldan, W.C. Kuster, D.C. Covert, and C.J. Hahn, The biogeochemical sulfur cycle in the marine boundary layer over the Northeast Pacific Ocean, *J. Atmos. Chem.*, **10**, 59–81, 1990.
- Bates, T.S., B.J. Huebert, J.L. Gras, B. Griffiths, and P. Durkee, The International Global Atmospheric Chemistry (IGAC) Project's First Aerosol Characterization Experiment (ACE 1): Overview, *J. Geophys. Res.*, this issue (a).
- Bates, T.S., V.N. Kapustin, P.K. Quinn, D.S. Covert, D.J. Coffman, C. Mari, P.A. Durkee, W.J. DeBruyn, and E. Satzman, Processes controlling the distribution of aerosol particles in the marine boundary layer during ACE 1, *J. Geophys. Res.*, this issue (b).
- Bechtold, P., C. Fravallo, and J.P. Pinty, A model of marine boundary layer cloudiness for mesoscale applications, *J. Atmos. Sci.*, **49**, 1723–1744, 1992.
- Bechtold, P., S.K. Krueger, W.S. Lewellen, E. Van Meijgaard, C.-H. Moeng, D.A. Randall, A. Van Ulden, and S. Wang, Modeling a stratocumulus-topped PBL: Intercomparison among different one-dimensional code with large eddy simulation, *Bull. Am. Meteorol. Soc.*, **77**, 2033–2042, 1996.
- Benkovitz, C.M., C.M. Berkovitz, R.C. Easter, S. Nemesure, R. Wagener, and S. Schwartz, Sulfates over the North Atlantic and adjacent continental regions: Evaluation for October and November 1986 using a three-dimensional model driven by observation-derived meteorology, *J. Geophys. Res.*, **99**, 20,725–20,756, 1994.
- Benkovitz, C.M., and S.E. Schwartz, Evaluation of modeled sulfate and SO₂ over North America and Europe for four seasonal months in 1986–1987, *J. Geophys. Res.*, **102**, 25,305–25,338, 1997.
- Berresheim, H., Biogenic sulfur emissions from the Subantarctic and Antarctic Oceans, *J. Geophys. Res.*, **92**, 13,245–13,262, 1987.
- Berresheim, H., M.O. Andreae, G.P. Ayers, R.W. Gillett, J.T. Merrill, V.J. Davis, and W.L. Chameides, Airborne measurements of dimethylsulfide, sulfur dioxide, and aerosol ions over the Southern Ocean south of Australia, *J. Atmos. Chem.*, **10**, 341–370, 1990.
- Berresheim, H., P. Wine, and D. Davis, in *Sulfur in the Atmosphere*, edited by H. Singh, pp 251–307, Van Nostrand Reinhold, New York, 1995.
- Bougeault, P., Modeling the trade-wind cumulus boundary layer. Part I: testing the ensemble cloud relations against numerical data, *J. Atmos. Sci.*, **38**, 2414–2428, 1981.
- Bougeault, P., and P. Lacarrère, Parameterization of orography-induced turbulence in a meso-beta scale model, *Mon. Weather Rev.*, **117**, 1872–1890, 1989.
- Brost, R.A., R.B. Chatfield, J. Greenberg, P.L. Haagenson, B. Heikes, S. Madronich, B. Ridley and P.R. Zimmerman, Three-dimensional modeling of transport of chemical species from continents to the remote Atlantic Ocean, *Tellus B*, **40B**, 358–379, 1988.

- Brost, R.A. and R.B. Chatfield, Transport of radon in a three-dimensional, subhemispheric model, *J. Geophys. Res.*, **94**, 5095–5119, 1989.
- Chang, J.S., R.A. Brost, I.S.A. Isaksen, S. Madronich, P. Middleton, W.R. Stockwell and C.J. Walcek, A Three-dimensional Eulerian Acid Deposition Model: physical concepts and formulation, *J. Geophys. Res.*, **92**, 14681–14700, 1987.
- Charlson, R.K., J.E. Lovelock, M.O. Andreae, and S.G. Warren, Oceanic phytoplankton, atmospheric sulphur, cloud albedo, and climate, *Nature*, **326**, 655–661, 1987.
- Chatfield, R.B., and P.J. Crutzen, Sulfur dioxide in remote oceanic air: Cloud transport of reactive precursors, *J. Geophys. Res.*, **89**, 7111–7132, 1984.
- Chin, M., D.J. Jacob, G.M. Gardner, M.S. Foreman-Fowler, and P.A. Spiro, A global three-dimensional model of the tropospheric sulfate, *J. Geophys. Res.*, **101**, 19667–18690, 1996.
- Chin, M., R.B. Rood, D.J. Allen, M.O. Andreae, A.M. Thompson, S.-J. Lin, R.M. Atlas, and J.V. Ardizzone, Processes controlling dimethyl sulfide over the ocean: Case studies using a 3-D model driven by assimilated meteorological fields, *J. Geophys. Res.*, in press, 1998.
- Eisele, F.L., and P.H. McMurry, Recent progress in understanding particle nucleation and growth, *Philos. Trans. R. Soc. London, Ser. B* **352**, 191–200, 1997.
- Erickson, D.J., III, S.J. Ghan, and J.E. Penner, Global ocean-to-atmosphere dimethylsulfide flux, *J. Geophys. Res.*, **95**, 7543–7552, 1990.
- Erickson, D.J. III, A stability dependent theory for air-sea gas exchange, *J. Geophys. Res.*, **98**, 8471–8488, 1993.
- Feichter, J., E. Kjellstrom, H. Rodhe, F. Dentener, J. Lelieveld, and G.-J. Roelofs, Simulation of the tropospheric sulfur cycle in a global climate model, *Atmos. Environ.*, **30**, 1693–1707, 1996.
- Ferek, R.J., R.B. Chatfield and M.O. Andreae, Vertical distribution of dimethylsulphide in the marine atmosphere, *Nature*, **320**, 514–516, 1986.
- Fouquart, Y., J.C. Buriez, M. Herman, and R.S. Kandel, The influence of clouds on radiation: A climate-modeling perspective, *Rev. Geophys.*, **28**(2), 145–166, 1990.
- Hainsworth, A.H.W., A.L. Dick, and J.L. Gras, Climatic context of ACE 1: A meteorological and chemical overview, *J. Geophys. Res.*, this issue.
- Huebert, B.J., S.G. Howell, L. Zhuang, J. Heath, M. Litchy, D.J. Wylie, J. Kreidel, S. Coeppicus and J. Pfeiffer, Filter and impactor measurements of anions and cations during ACE 1, *J. Geophys. Res.*, this issue.
- Hynes, A.J., P.H. Wine, and D.H. Semmes, Kinetics and mechanism of OH reactions with organic sulfides, *J. Phys. Chem.*, **90**, 4148–4156, 1986.
- Kain, J.S., and J.M. Fritsch, A one-dimensional entraining/detraining plume model and its application in convective parameterization, *J. Atmos. Sci.*, **47**, 2784–2802, 1990.
- Lafore, J.P. et al., The Meso-NH atmospheric simulation system Part I. Adiabatic formulation and control simulations, *Ann. Geophys.*, **16**, 90–109, 1998.
- Langner, J., and H. Rodhe, A global three-dimensional model of the tropospheric sulfur cycle, *J. Atmos. Chem.*, **13**, 225–263, 1991.
- Leck, C., and C. Persson, Seasonal and short-term variability in dimethyl sulfide, sulfur dioxide and biogenic sulfur and sea salt aerosol particles in the Arctic marine boundary layer during summer and autumn, *Tellus*, **48**, 272–299, 1996.
- Lipps, F.B., and R.S. Hemler, A scale analysis of deep moist convection and some related numerical calculations, *J. Atmos. Sci.*, **39**, 2192–2210, 1982.
- Liss, P.S., A.D. Hutton, G. Malin, P.D. Nightingale, and S.M. Turner, Marine sulphur emissions, *Philos. Trans. R. Soc. London, Ser. B*, **352**, 159–169, 1997.
- Liss, P.S., and L. Merlivat, Air-sea exchange rates: Introduction and synthesis, in *The Role of Air-Sea Exchange in Geochemical Cycling*, edited by P. Buat-Ménard, pp 113–127, D. Reidel, Norwell, Mass., 1986.
- Liu, S.C. et al., Model study of tropospheric trace species distributions during PEM-West A, *J. Geophys. Res.*, **101**, 2073–2085, 1996.
- Madronich, S., Photodissociation in the atmosphere, 1, Actinic flux and the effects of ground reflections and clouds, *J. Geophys. Res.*, **92**, 9740–9752, 1987.
- Morcrette, J.J., Physical parameterization of the ECMWF Model, ECMWF, Reading, 1989.
- Petersen, A.C., C. Beets, H. Van Dop, P.G. Duynkerke, and A.P. Siebesma, Mass-flux schemes for transport of non-reactive and reactive scalars in the convective boundary layer, *J. Atmos. Sci.*, in press.
- Pham, M., J.-F. Müller, G.P. Brasseur, C. Granier, and G. Mégie, A three-dimensional study of the tropospheric sulfur cycle, *J. Geophys. Res.*, **100**, 26061–26092, 1995.
- Pyle, J.A., and A.M. Zavody, The modelling problems associated with spatial averaging, *Q. J. R. Meteorol. Soc.*, **116**, 753–766, 1990.
- Ravishankara, A.R., Y. Rudich, R. Talukdar and S.B. Barone, Oxidation of atmospheric reduced sulphur compounds; perspective from laboratory studies, *Philos. Trans. R. Soc. London, Ser. B*, **352**, 171–182, 1997.
- Saltzman, E.S., D.B. King, K. Holmen, and C. Leck, Experimental determination of the diffusion coefficient of dimethylsulfide in water, *J. Geophys. Res.*, **98**, 16481–16486, 1993.
- Siebesma A.P. and J.W.M. Cuipers, Evaluation of parametric assumptions for shallow cumulus convection, *J. Atmos. Sci.*, **52**, 650–666, 1995.
- Smethie, W.M., T. Takahashi, D.W. Chipman, and J.R. Ledwell, Gas exchange and CO₂ flux in the tropical Atlantic Ocean determined from ²²²Rn and CO₂ measurements, *J. Geophys. Res.*, **90**, 7005–7022, 1985.
- Smolarkiewicz, P.K., Comment on "A positive definite advection scheme obtained by nonlinear renormalization of the advective fluxes", *Mon. Weather Rev.*, **117**, 2626–2632, 1989.
- Spivakovsky, C.M., R. Yevich, J.A. Logan, S.C. Wofsy, M.B. McElroy, and M.J. Prather, Tropospheric OH in a three-dimensional chemical tracer model: An assessment based on observations of CH₃CCL₃, *J. Geophys. Res.*, **95**, 18441–18471, 1990.
- Stull, R.B., *An introduction to Boundary Layer Meteorology*, Kluwer Acad., Norwell, Mass., 1988.
- Suhre, K., et al., Physico-chemical modeling of ACE 1 Lagrangian B, 1, A moving column approach, *J. Geophys. Res.*, this issue.
- Tans, P.P., Y. Fung, and T. Takahashi, Observational constraints on the global atmospheric CO₂ budget, *Science*, **247**, 1431–1438, 1990.
- Turner, S.M., G. Malin, P.D. Nightingale, and P.S. Liss, Seasonal variation of dimethyl sulphide in the North Sea and an assessment of fluxes to the atmosphere, *Mar. Chem.*, **54**, 245–262, 1996.
- Turnispeed, A.A., and A.R. Ravishankara, The atmospheric oxidation of dimethylsulfide: elementary steps in a complex mechanism, in *Dimethylsulphide: Oceans, Atmosphere and Climate*, edited by G. Restelli, and G. Angeletti, pp. 185–196, Kluwer Acad., Norwell, Mass., 1993.
- Wang, C., P. J. Crutzen, V. Ramanathan, and S. F. Williams, The role of a deep convective storm over the tropical Pacific Ocean in the redistribution of atmospheric chemical species, *J. Geophys. Res.*, **100**, 11509–11516, 1995.
- Wanninkhof, R., Relationship between wind speed and gas exchange over the ocean, *J. Geophys. Res.*, **97**, 7373–7382, 1992.
- Yin, F., D. Grossjean, and J.H. Seinfeld, Photooxidation of dimethyl sulfide and dimethyl disulfide, *J. Atmos. Chem.*, **11**, 309–399, 1990.

A. R. Bandy and D. C. Thornton, Department of Chemistry, Drexel University, Philadelphia, PA 19104.

T. S. Bates and J. E. Johnson, Pacific Marine Environmental Laboratory, NOAA, 7600 Sand Point Way NE, Seattle, WA 98115.

F. L. Eisele and L. Mauldin III, Atmospheric Chemistry Division, NCAR, Boulder, CO 80307.

C. Mari, R. Rosset, K. Suhre, Laboratoire d'Aérodynamique, UMR 5560 CNRS/Université Paul Sabatier, 31400 Toulouse, France. (e-mail: marc@aero.obs-mip.fr)

(Received October 27, 1997; revised March 30, 1998; accepted March 31, 1998.)